IEEE Access
Multidisciplinary | Rapid Review | Open Access Journal

Received May 12, 2020, accepted June 4, 2020, date of publication June 9, 2020, date of current version June 19, 2020.

Digital Object Identifier 10.1109/ACCESS.2020.3001066

Strain Rate Effect on the Mechanical Properties and Fracture Surface Roughness of Sandstone Subjected to Dynamic Direct Tension

YANLONG CHEN[1], GANG LIN[2], RONGRONG MAO[1,3], MING LI[1], XIANBIAO MAO[2], AND KAI ZHANG[1]

[1]State Key Laboratory for Geomechanics and Deep Underground Engineering, China University of Mining and Technology, Xuzhou 221116, China
[2]School of Mechanics and Civil Engineering, China University of Mining and Technology, Xuzhou 221116, China
[3]Department of Ship and Marine Engineering, Nantong Shipping College, Nantong 226010, China

Corresponding authors: Gang Lin (ts18030025a31@cumt.edu.cn) and Rongrong Mao (rongrmao@163.com)

This work was supported in part by the Fundamental Research Funds for the Central Universities under Grant 2019XKQYMS53.

ABSTRACT Dynamic properties of rocks are extremely important in a variety of rock mechanics and rock engineering problems. The split Hopkinson tensile bar (SHTB) system is used in this paper to measure the mechanical properties of sandstone specimens under dynamic direct tension, and the full stress-strain curves of the specimens at different strain rates is obtained. The experimental results indicate that the tensile strength, the tensile modulus and the peak strain of the specimen increase almost linearly with the strain rate. The increases in the tensile strength, the tensile modulus and the peak strain reach 125 %, 37 % and 98 % respectively as the strain rate increases by 252 %. The microscopic structure characteristics of the fracture surfaces after the tensile failure of the specimens are investigated by three-dimensional scanning. The results suggest that the fracture surface roughness of the sandstone under direct tension is significantly sensitive to the strain rate. Both the roughness coefficient and the fractal dimension of the specimen increase with the strain rate. The fracture surface of the specimen changes from a relatively flat two-dimensional state to a three-dimensional state, and its relative area gradually increases. Finally, it is manifested from the aspect of energy consumption that both the energy consumed in the fracture process and the dynamic direct tensile strength enhance with the fracture surface roughness. It is believed that the investigation results can provide an important reference for the research on dynamic properties of rocks involved in experimental research and engineering practice.

INDEX TERMS Dynamic properties, split Hopkinson tensile bar, direct tension, strain rate, fracture surface roughness.

I. INTRODUCTION

The accurate determination of rock dynamic properties has always been an important issue for rock engineering and mining engineering [1]. Its applications include rock mass excavation, the prediction of rock bursts and earthquakes, drilling and blasting, projectile penetrations, etc [2]. Rocks are brittle materials and have tensile strength much lower than their compressive strength [3]. Tensile failure normally occurs in rocks under external loading, and the failure process is highly sensitive to the strain rate of the external loading [4], [5]. Therefore, it is of great significance to understand the mechanical properties of rocks under dynamic tension in order for rock breaking and rock support.

Due to the difficulty in the direct measurement of the mechanical properties of rocks under tension, the Brazilian disc test has become the main static method for the indirect measurement of the tensile properties of rocks [6]–[8]. Based on the static test method, the split Hopkinson pressure bar (SHPB) has been developed to perform dynamic indirect tensile tests on disc shaped specimens. It is found by many authors that the mechanical characteristics of rocks under dynamic tension highly depend on the strain rates of the external loading [9]–[11]. Besides, the mechanical characteristics of rocks under dynamic tension were indirectly measured by some authors with three-point bending tests [12]–[14].

The associate editor coordinating the review of this manuscript and approving it for publication was Laurence T. Yang.

However, the results from the previous studies indicated that some shortcomings still exist in the indirect tension tests of rocks. The specimens could initially sustain compressive stresses (rather than tensile stresses), and the stress conditions in the experiments could be non-uniform. Hence it is difficult to ensure that the specimens were always under uniaxial tension in previous studies [15], [16].

In order to more accurately obtain the tensile properties of rocks, some authors conducted static direct tension tests to realize the direct tension of rock specimens. Two main methods have been commonly used to prepare the specimens in the static direct tension tests. First, irregular shaped specimens, such as the bone-shaped specimens [17], can be used to simulate the tensile stresses in the specimens. In this case, the specimens are under external compressive loading. Second, special clamping systems or loading fixtures are designed to directly apply the external tensile loading to the specimens. Li *et al.* [18] developed a clamping system (in which nuts are used to fix the specimens) to study the tensile characteristics of gypsum specimens and plate-shaped granite specimens. Saiang *et al.* [19] designed a specific loading fixture to realize the direct tension of concrete specimens. Zhang *et al.* [20] eliminated the dislocation of direct tensile loading in their experiments with a self-developed centring device. Unlu and Yilmaz [21] innovated a push-pull direct tensile strength testing apparatus to measure the direct tensile strength of cylindrical rock specimens. Liu *et al.* [22] designed a tension-compression cyclic measurement system based on the material testing system (MTS). Hashiba *et al.* [23] discussed the compatibility between the specimen and the clamping system in the direct tension test and proposed the design requirement for the clamping system of brittle rocks. In addition, some authors used powerful glue to attach the specimen to the MTS in order to perform the direct tension test.

Compared with static direct tension, it is more difficult to realize the dynamic direct tension of rocks in laboratory experiments. The dynamic tensile characteristics of rocks under direct tension have been studied by numerical modelling for a long time. Nevertheless, experimental results are still required as the benchmarks for the validation of the numerical modelling results [24], [25]. Recently, with the development of the testing system and the loading method, experimental apparatuses that aim at providing dynamic direct tension to rock specimens at high strain rates have been developed, in which the most representative one is the split Hopkinson tensile bar (SHTB) system. Cadoni [26] studied the effects of the strain rate on the direct tensile strength of orthogneiss specimens with the SHTB system and revealed the influence of the loading direction on the tensile strength. Kong *et al.* [27] established a non-local damage constitutive model for the dynamic direct tension of concrete and validated its applicability through direct tension tests on concrete specimens with the SHTB system.

A fracture surface forms when the rock fails under dynamic direct tension. The geometry of the fracture surface reflects the fracture process and is significant to the deduction of the stress environment at the fracture surface in the fracture process [28]. Previous studies on the roughness of a discontinuity focused on the shear-resisting characteristics of the rock mass. The joint roughness coefficient (JRC) was proposed by Barton [29] and has been further extended by El-Soudani [30], Maerz *et al.* [31] and El-Soudani [30] etc. In recent year, studies on the influence of discontinuity roughness on fluid flow in jointed rock mass and the strength and energy consumption of the discontinuity in the fracture process have become increasingly popular [7], [24], [33]. The method proposed by Tse and Cruden [34] was mainly used in previous studies for the characterization of the roughness of the discontinuity [22], [35], [36]. This method divides the discontinuity into several equidistant lines along its length direction to extract a certain amount of two-dimensional sections. The discontinuity roughness is described by calculating the ratios of the cross section line length of these two-dimensional sections to their projected length. However, Tse and Cruden's method [34] is basically the two-dimensional simulation of the roughness of the fracture surface. To better understand the geometry of a three-dimensional fracture surface, the three-dimensional characteristics at the fracture surface need to be quantified.

Though the experimental system for the dynamic direct tension test on the rock develop rapidly, it is difficult to limit the fracture location of a brittle material at the middle part of the specimen. This causes the low success rate of the experiment. Therefore, research results of dynamic direct tension tests on rock-like brittle materials have been rarely reported. Moreover, the understanding of the fracture mechanism of dynamic direct tension from the aspect of fracture roughness remains unclear.

The SHTB system is used in this paper to successfully conduct dynamic direct tension tests on sandstone. The effects of the strain rate on the mechanical characteristics of sandstone under dynamic direct tension are analyzed. Based on the joint roughness scanning results, it is found that the roughness of the fracture surface of the sandstone specimen under direct tension is also sensitive to the strain rate. Finally, the relation between the fracture roughness and the energy consumption in the tensile failure process is disclosed. The research outcomes in this paper will provide an important reference for the research on dynamic properties of rocks in numerous rock engineering areas.

II. EXPERIMENTS

A. DYNAMIC DIRECT TENSION EXPERIMENT

1) SPECIMEN PREPARATION

The sandstone specimens used in this paper are collected from the roof rock mass at an underground coal mine. The physical and static mechanical parameters of the rock specimens are shown in Table 1.The specimen mainly contains quartz (10.8 %), kaolinite (11.6 %), potash feldspar (4.5 %)

TABLE 1. The physical and static mechanical parameters of the sandstone specimen.

Density ($kg \cdot m^{-3}$)	Porosity (%)	Uniaxial compressive strength (MPa)	Elasticity modulus (GPa)	Poisson's ratio	Tensile strength (MPa)
2410	1.09	113.59	9.44	0.21	3.88

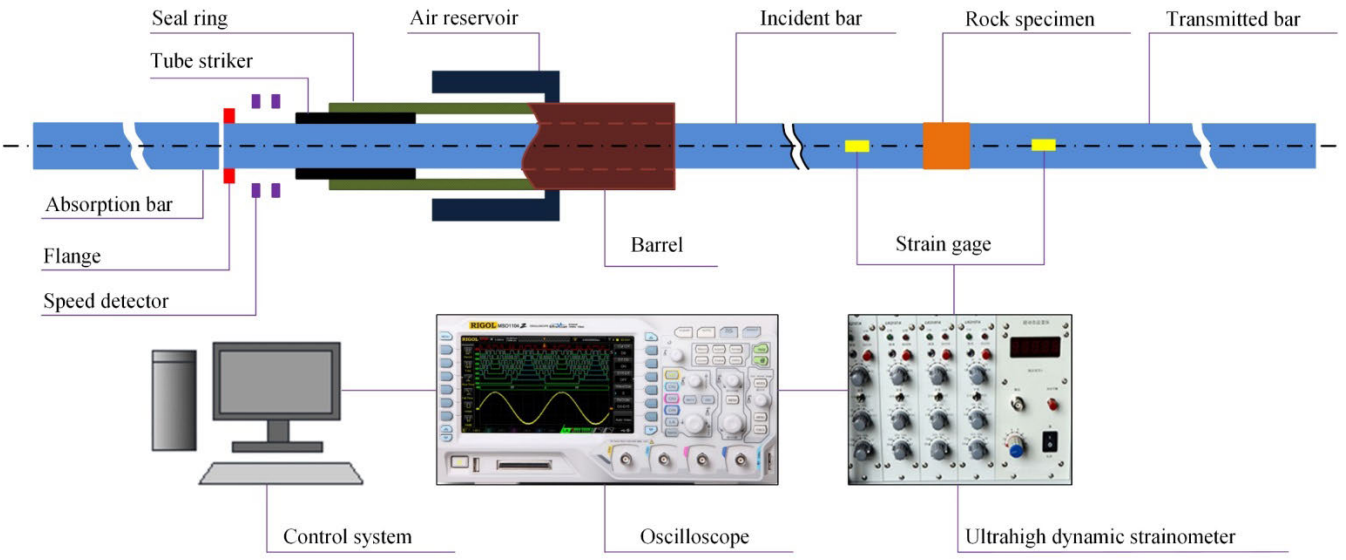

FIGURE 1. Schematic diagram of a SHTB experimental system.

and calcium feldspar (73.0 %). Each specimen has dimensions of 20 mm (in diameter) × 20 mm (in height) in order to fit the experimental system. The specimens are prepared according to the following procedures. First, specimens are cored from sandstone samples and cut and grinded to standard dimensions (50 mm (in diameter) × 100 mm (in height)) based on the method suggested by the International Society of Rock Mechanics (ISRM). Second, an ultrasonic instrument is used to detect the wave velocities of the standard specimens. The specimens with similar wave velocities are selected. Third, the specimens with the diameter of 20 mm are cored from the standard specimens with a drilling bit (which also has the diameter of 20 mm). The specimens are then cut and grinded to the dimensions of 20 mm (in diameter) × 20 mm (in height). Finally, the ultrasonic instrument is used to measure the wave velocities of the processed specimens. The specimens that have similar wave velocities to the standard specimens are selected as the final specimens used in the laboratory experiments in this paper.

2) EXPERIMENTAL SYSTEM

The incident bar and the transmission bar in the SHTB system used in this study have the diameter of 20 mm (Figure 1). The SHTB system mainly consists of the energy-driven components (the tube striker, seal ring, air reservoir, the barrel and the flange), the bar components (the incident bar and the transmission bar), the data collection and processing components (the ultrahigh dynamic strainometer, the oscilloscope and the control system) and the energy absorption components (the absorbing bar). The specimen is placed between the incident bar and the transmission bar before the experiment.

The tube striker hits the flange in each test, driven by the high pressure gas. Then compression pulses form at the flange and reflected tensile stress waves and transmission waves are generated at the free end of the flange. The reflected tensile stress waves are transmitted through the incident bar to the specimen and reflect and transmit several times at the interface between the specimen and the incident bar and the interface between the specimen and the transmission bar. This causes the tensile failure of the specimen at a high strain rate. Meanwhile, parts of the pulses are reflected, and the others are transmitted to the incident bar through the specimen and become reflected pulse signals and transmission pulse signals. The pulse signals are recorded by the signal collection system through the strain gages attached to the incident bar and the transmission bar. The stress pulse data is then processed by the data processing system to derive the experimental results of the tension test on the sandstone specimen at a high strain rate.

3) SPECIMEN INSTALLATION

The core of the dynamic direct tension of a rock specimen is the scientific, effective installation of the specimen between

the incident bar and the transmission bar. Irregular specimens and self-developed clamping systems are used to realize the direct tension of rock specimens in previous studies. These approaches achieved quite good experimental results in static tension tests on rocks but had poor performance in dynamic tension tests. At present, the most scientific, reasonable method is to bond the specimen to the bar components, which is adopted in this paper for the installation of the sandstone specimen in the dynamic direct tension test.

a: SPECIMEN CEMENTATION

The reasonable selection of the adhesive is basic to the successful installation of the specimen. The efficiency of three different types of adhesives is compared in the experiment, including the cyanoacrylate glue, the ordinary two-component adhesive and the super two-component adhesive. The cyanoacrylate glue is found to be effective in boding the specimen to the bar components in a relatively short time but has poor moisture resistance due to which the specimen detaches from the bar components after 2 hours adhesion. Besides, the cyanoacrylate glue has relatively low adhesive strength. Though the ordinary two-component adhesive has higher adhesive strength than cyanoacrylate glue, the specimen tends to detach from the bar components (rather than fail at the middle part of the specimen) in the direct tension test if the ordinary two-component adhesive is used. In addition, a film of the ordinary two-component adhesive forms at the specimen-bar interface and affects the transmission of the stress wave. The super two-component adhesive is able to securely bond the specimen to the bar components, and its adhesive strength is much higher than the tensile strength of the specimen. Moreover, no adhesion layer forms at the specimen-bar interface when the watery acrylate adhesive is used. The super two-component adhesive reaches 70 % and 100 % of its ultimate strength after 10 hours and 12 hours adhesion respectively.

b: SPECIMEN FIXATION

According to the observation on a series of experiments, it is found that the fracture surfaces of the specimens are usually very close to the specimen-bar interfaces (i.e. the adhesives) as shown in Figure 2. The reason is that the part of the specimen close to the specimen-bar interface is under a non-uniform triaxial tensile stress condition and its lateral deformation is restricted due to the adhesion between the specimen surface and the bar surface.

In order to make the specimen fails at its middle part, the reinforcement of the specimen is required. After the specimen is bonded to the bar components by the acrylate adhesive, multilayer steel wire gauze is adhered to the part of the specimen close to the specimen-bar interface. No steel wire gauze is adhered to the middle part of the specimen, and the number of the layers of the steel wire gauze gradually increases at the part of the specimen closer to the specimen-bar interface (Figure 3a). This is to ensure that the middle part of the specimen is under uniaxial tension, which improves the success rate of the experiment. Figure 3b shows a failed specimen under dynamic tension.

FIGURE 2. The fracture surface of a specimen under specimen unreinforcement.

4) EXPERIMENTAL SCHEMES

The experiments aim at understanding the influence of the strain rate on the mechanical characteristics of the sandstone specimen under dynamic direct tension. Hence high pressure gases with different magnitudes are used to conduct the direct tension tests. It is found that the minimum impact pressure of 0.15 MPa is required to fracture the specimen under direct tension. Since the dynamic direct tension test is more sensitive to the strain rate compared with the compression test, a small interval of the high pressure gas is designed in this study. The experiments consist of 6 different test scenarios in which the gas pressure magnitudes increase from 0.15 MPa to 0.20 MPa at an interval of 0.01 MPa. Each test scenario is repeated several times (i.e. each test scenario has several test cases under the same experimental condition), and the strain rate in each test case is calculated by the three-wave method [37], [38]. To minimize the experimental error, the results of the three test cases that have similar strain rates in each test scenario are analyzed in the following context.

In each test, the sheet rubber with dimensions of 5.0 mm (in diameter) $\times$ 1.0 mm (in thickness) is used as the waveform shaper [9], [39] for waveform correction (Figure 4a). Figure 4b compares the waveforms before and after the correction of the waveform shaper. The incident wave of the corrected waveform has a half-sine waveform and the stress wave shows no obvious transversal oscillation in the transmission process.

A typical waveform of the sandstone specimen under dynamic direct tension is given in Figure 5. It shows that the half-sine waveform dominates the waveforms of the incident wave, the reflected wave and the transmitted wave. The amplitude of the transmitted wave is much lower than the incident wave and the reflected wave, and no obvious transversal oscillation is observed during the transmission of the stress wave. The experiment basically provides a one-dimensional stress state to the specimen. The incident

FIGURE 3. The fracture surfaces of a specimen under specimen reinforcement. (a) before tensile failure; (b) after tensile failure.

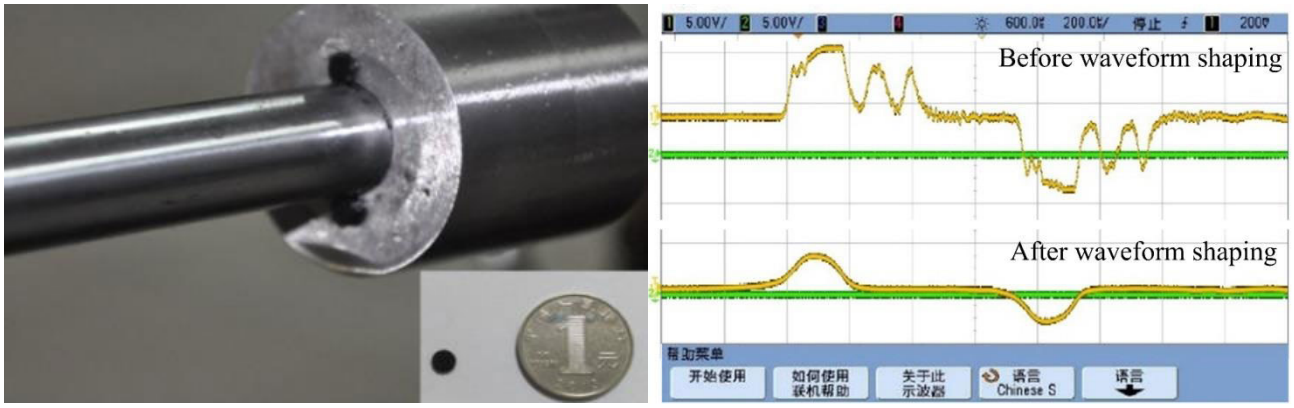

FIGURE 4. The method and effect of wave shaping for shock stress wave in dynamic tensile test. (a) installation of the pulse shaper; (b) effect of wave shaping.

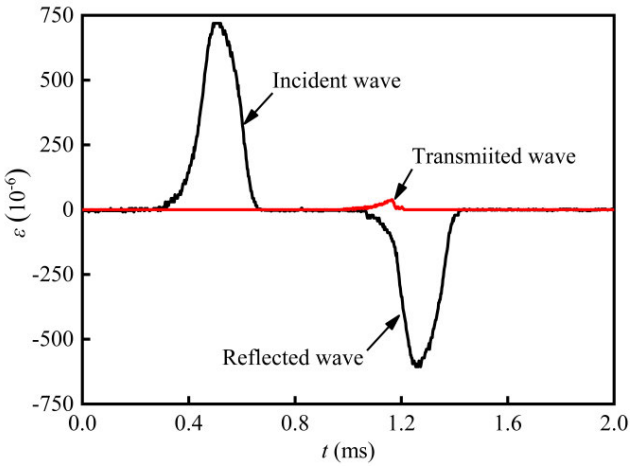

FIGURE 5. A typical waveform of the sandstone specimen under dynamic direct tension.

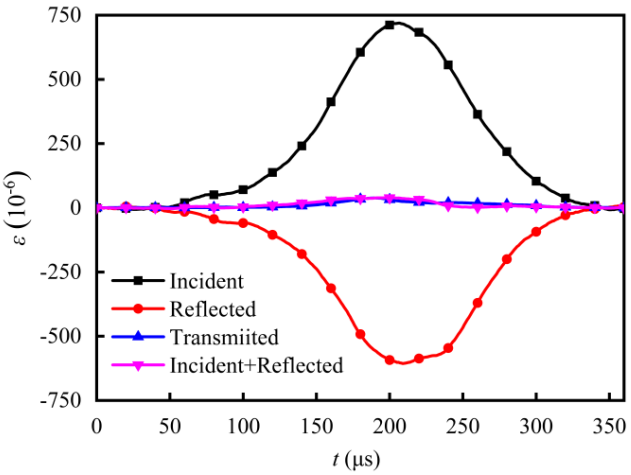

FIGURE 6. The Verification of the stress equilibrium in SHTB test.

wave takes 100 μs to reach its amplitude, which gives the stress wave sufficient time for its repeated transmission in the specimen and favours the formation of a uniform stress state in the specimen.

In SHTB tests, the stress equilibrium at both sides of the specimen requires careful examination [40]. Figure 6 suggests that the superimposition of the incident wave and the reflected wave approximately coincides with the transmission

wave, which proves that the stress equilibrium at both sides of the specimen are achieved.

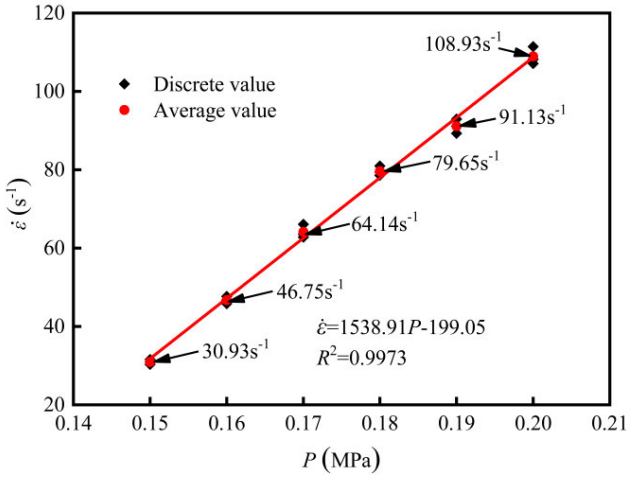

FIGURE 7. The variation of loading strain rate with impact loading pressure.

Figure 7 shows the influence of the impact loading pressure on the strain rate of the dynamic tension test. The strain rates in the test cases in the same test scenario approximate to each other. Figure 7 also gives the average strain rate in each test scenario, which increases with the loading pressure.

B. SCANNING OF FRACTURE SURFACES OF SANDSTONE SPECIMENS AFTER THEIR TENSILE FAILURES

The scanning electron microscope (SEM) is used to scan the fracture surfaces of the sandstone specimens in order to disclose the failure mechanism of the specimens under direct tension at high strain rates and reveal the microscopic structure characteristics of the fracture surfaces at different strain rates.

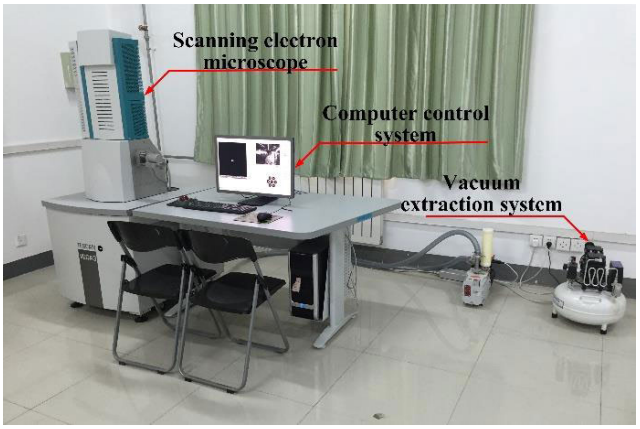

FIGURE 8. SEM experimental system and its structure composition.

The TESCAN VEGA3 type SEM system is used in this experiment (Figure 8). The experimental system consists of three components, including the SEM, the computer control system and the vacuum extraction system. The SEM is the key component, which is composed of the electron optical system, the scannig system, the signal receiving and displaying system and the specimen moving system.

The sample is collected from the fracture surface, made into a round disc with dimensions of 10 mm (in diameter) × 2 mm (in thickness) and installed to the specimen panel in the specimen chamber. The specimen chamber is closed and the vacuum extraction system is operated to evacuate the specimen chamber to the air pressure of 10^{-4} Pa. In the scanning process, electron beams are emitted from an electron gun. The electron beams are focused by a grid and pass through the electron optical system (which consists of two to three electromagnetic lenses) under the effect of accelerating voltage. Then the electron beams become a thin electron beam and focuses on the specimen surface. Various information is generated by the interaction between the high-energy electron beam and the specimen substance, and finally the microscopic structure characteristics of the specimen surface are derived.

III. RESULTS

A. STRESS-STRAIN CURVES OF SANDSTONE SPECIMENS UNDER DYNAMIC DIRECT TENSION

Based on the propagation theory of one-dimensional elastic wave [9], the stress, strain and average strain rate can be calculated by equation (1), equation (2) and equation (3), respectively.

$$\sigma(t) = \frac{A}{A_0} E \varepsilon_t(t) \tag{1}$$

$$\varepsilon(t) = -\frac{2C}{L} \int_0^t \varepsilon_r(t) \mathrm{d}t \tag{2}$$

$$\dot{\varepsilon}(t) = -\frac{2C}{L} \varepsilon_r(t) \tag{3}$$

where A is the cross sectional area of the pressure bar, A_0 is the cross sectional area of the sample, E is the elastic moduli of the pressure bar, C is the elastic wave velocity of the pressure bar; L is the length of the sample, ε_t is the transmitted strain and ε_r is the reflected strain.

Based on the processing of the waveforms from the test results [16], the stress-strain curves of the sandstone specimens under dynamic direct tension at different strain rates are provided in Figure 9. Compared with the results in Figures 9a to 9f, the shapes of the stress-strain curves of the specimens at different strain rates are similar to each other. The differences in the stress-strain curves include the peak strength, the peak strains (i.e. the strains at which the strength failure of the specimens occurs) and the dynamic tensile moduli. As shown in Figure 9, the stress-strain curve of the specimen under dynamic direct tension at a high strain rate can be divided into the following four stages.

1) THE ELASTIC DEFORMATION STAGE (I)

The specimen deforms elastically at the early stage of the dynamic tensile loading. The stress increases linearly and

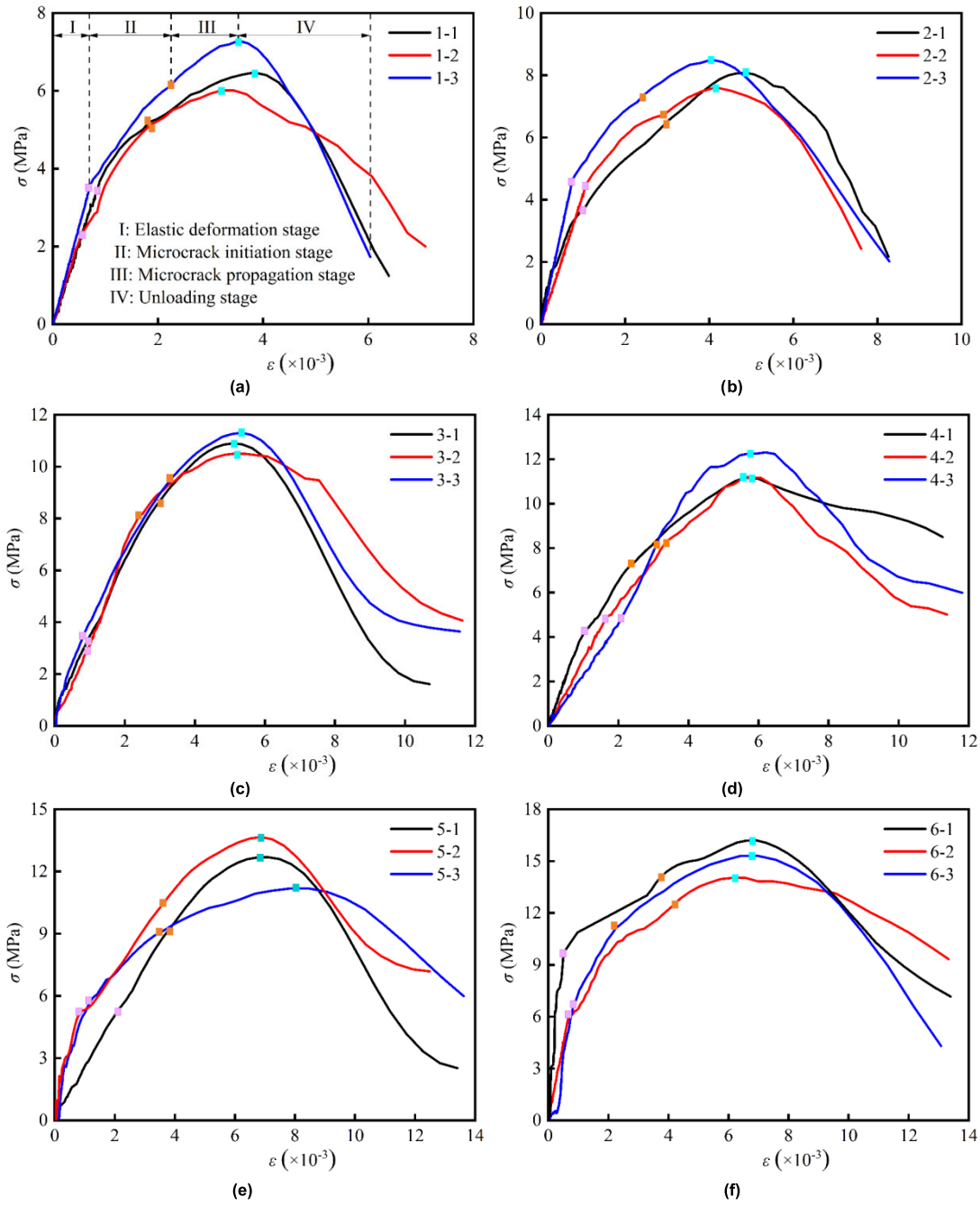

FIGURE 9. Direct tension stress-strain curves of sandstone in different strain rate. (a) the strain rate is 30.93s^{-1}; (b) the strain rate is 46.75s^{-1}; (c) the strain rate is 64.14s^{-1}; (d) the strain rate is 79.65s^{-1}; (e) the strain rate is 91.13s^{-1}; (f) the strain rate is 108.93 s^{-1}.

rapidly with the strain, and the relation between the stress and the strain can be described by Equation (4):

$$d^2\sigma/d\varepsilon^2 = 0 \tag{4}$$

where σ is the stress and ε is the strain. The stress wave repeated reflects in this stage, and the stress increment becomes stabilized. The elastic energy in the specimen gradually accumulates. The slope of the stress-strain curve in the elastic deformation stage maintains constant and is normally considered as the dynamic tensile modulus of the specimen.

2) THE MICROCRACK INITIATION STAGE (II)

After the elastic deformation stage, the energy stored in the specimen begins to induce the initiation and propagation of the microcracks. The slope of the stress-strain curve slowly declines due to the initiation of the microcracks at some

existing defects and weak planes. The second stage lasts for a quite long time in the experiment, and the stable propagation of the microcracks causes the gradual decrease of the slope as described in Equation (5).

$$d^2\sigma/d\varepsilon^2 < 0 \tag{5}$$

3) THE MICROCRACK PROPAGATION STAGE (III)

The elastic energy in the specimen releases quickly in this stage. The existing and the newly-formed microcracks in the specimen propagate unstably and interact with each other to form the macroscopic fracture planes that stretch through the specimen. The slope of the stress-strain curve decreases rapidly and approaches zero at the end of this stage. The stress reaches the ultimate load-bearing capacity of the specimen. The expression of the slope in the third stage in given in Equation (6), and the description of the slope when the specimen fails is provided in Equation (7).

$$d^2\sigma/d\varepsilon^2 \leq 0 \tag{6}$$

$$d\sigma/d\varepsilon = 0 \tag{7}$$

4) THE UNLOADING STAGE (IV)

The stress in this stage drops fast at a certain slope as the strain increases, and the specimen gradually loses its load-bearing capacity. Besides, no residual deformation is found in the stress-strain curve. The relation between the stress and the strain in the fourth stage is given in Equation (8).

$$d\sigma/d\varepsilon < 0 \tag{8}$$

The stress-strain curves of the sandstone specimens under dynamic direct tension at different strain rates are provided in Figure 9.

B. MECHANICAL PROPERTIES OF SANDSTONE SPECIMENS UNDER DYNAMIC DIRECT TENSION

Based on the stress-strain curves of the specimens under dynamic direct tension, the mechanical properties of the specimens at different strain rates are derived, including the dynamic tensile strength (σ_T), the dynamic tensile moduli (E_T) and the dynamic peak strain (ε_T). The changes of these properties with the strain rate ($\dot{\varepsilon}$) are given in Figure 10. It is found that all these three properties increase linearly with the strain rate.

1) VARIATION CHARACTER OF THE DYNAMIC TENSILE STRENGTH

As shown in Figure 9a, the dynamic tensile strength of the specimen increases linearly with the strain rate. The dynamic tensile strength increases by 125 % (from 6.59 MPa to 14.85 MPa) when the strain rate increases by 252 % (from 30.93 s^{-1} to 108.93 s^{-1}). Hence the ultimate strength of the specimen under dynamic tension increases with the strain rate.

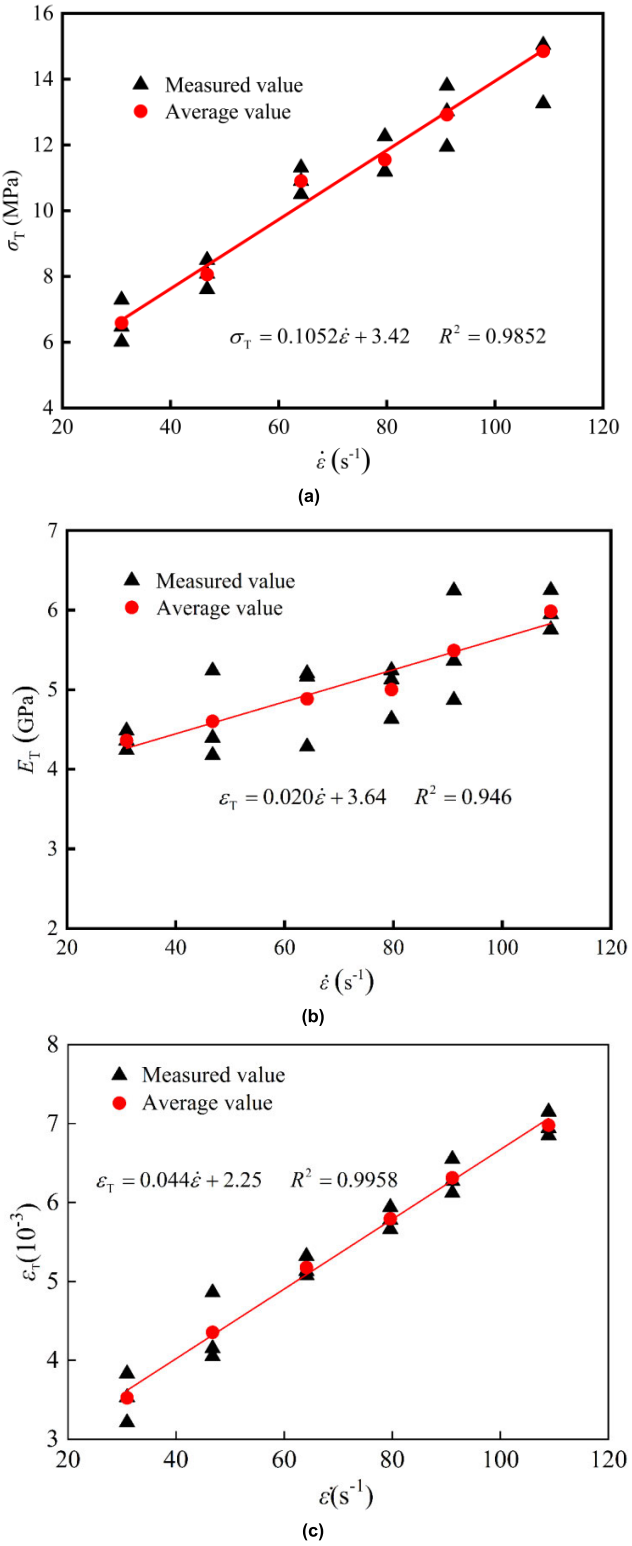

FIGURE 10. The changes of mechanical properties of the specimens with the strain rate. (a) dynamic tensile strength; (b) dynamic tensile moduli; (c) dynamic peak strains.

2) VARIATION CHARACTER OF THE DYNAMIC TENSILE MODULI

Figure 9b indicates that the dynamic tensile modulus of the sandstone specimen increases linearly with the strain rage.

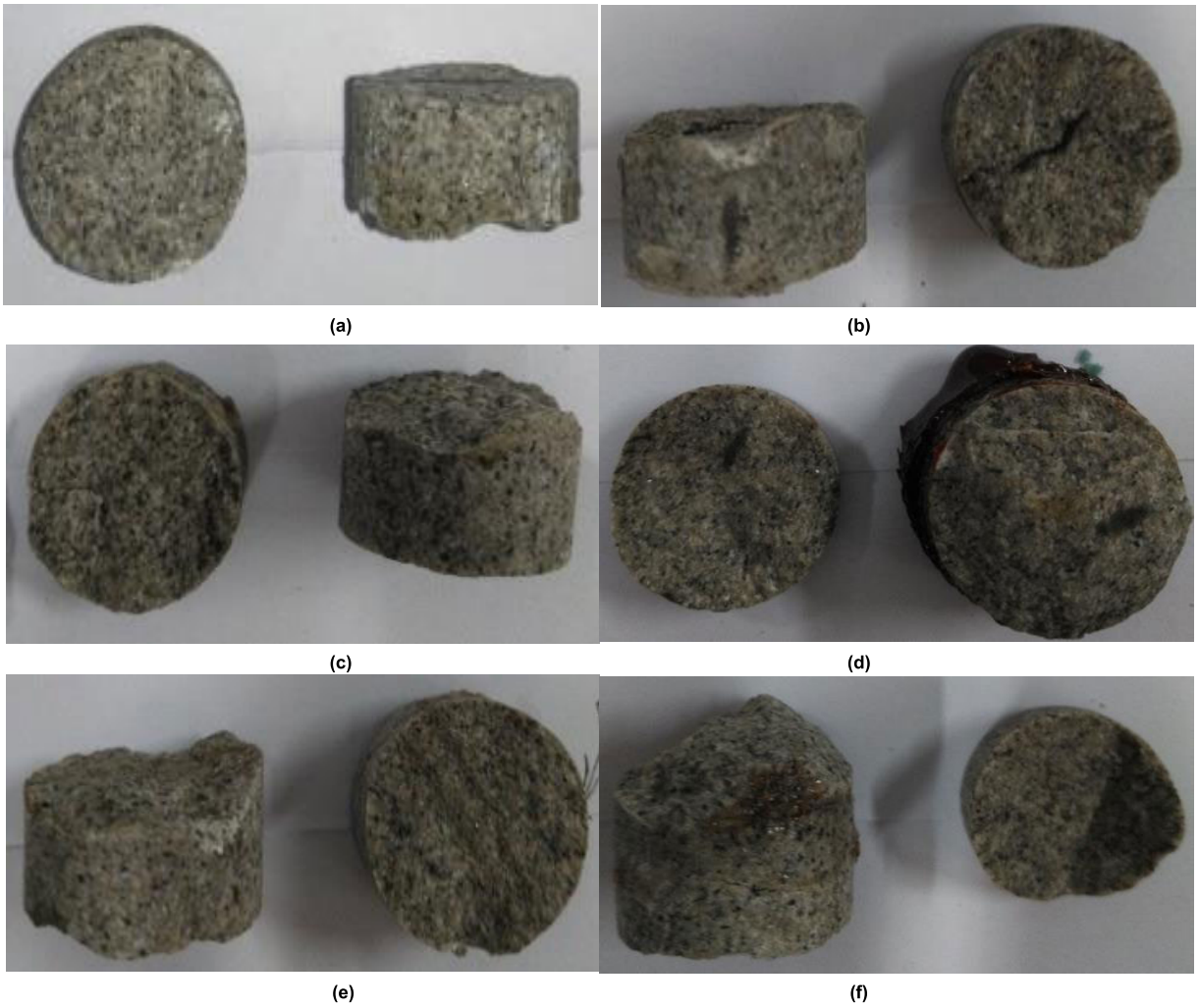

FIGURE 11. The macroscopic characteristics of the fracture surfaces of the specimens under direct tension at different strain rates. (a) the strain rate is 30.93s^{-1}; (b) the strain rate is 46.75s^{-1}; (c) the strain rate is 64.14s^{-1}; (d) the strain rate is 79.65s^{-1}; (e) the strain rate is 91.13s^{-1}; (f) the strain rate is 108.93 s^{-1}.

The dynamic tensile modulus increases by 37 % (from 4.36 GPa to 5.98 GPa) when the strain rate increases by 252 % (from 30.93 s^{-1} to 108.93 s^{-1}). Therefore, the deformability of the rock improves at a higher strain rate.

3) VARIATION CHARACTER OF THE DYNAMIC PEAK STRAIN

Figure 9c suggests that the dynamic peak strain of the specimen almost changes linearly with the strain rate. It increases by 98 % (from 3.52× 10^{-3} to 6.98× 10^{-3}) when the strain rate increases by 252 % (from 30.93 s^{-1} to 108.93 s^{-1}). The ultimate deformability of the rock enhances with the increase of the strain rate.

C. CHARACTERISTICS OF FRACTURE SURFACES OF SANDSTONE SPECIMENS UNDER DYNAMIC TENSION

Figure 11 shows the macroscopic characteristics of the fracture surfaces of the specimens under direct tension at different strain rates. Microscopic observation is an important method to characterize rock mass morphology [41], [42]. Figure 12 gives the microscopic characteristics of the fracture surfaces observed from SEM scanning (with 10-time-magnification). Similar to the failure mode of the rock under static tension, the rock under dynamic tension at a high strain rate ruptures into two parts. Despite the existence of a small angle between the normal direction of the fracture surface and the specimen axis, the specimen generally fails in tension along its axis (i.e. the fracture surface is perpendicular to the specimen axis).

Figures 11 and 12 indicate that the fracture surfaces look flat when the strain rates are 30.93 s^{-1} and 46.75 s^{-1}. No local fracture surface (that is formed by secondary fractures) or obvious shadow area is observed in the images. When the strain rates increase to 64.14 s^{-1} and 79.65 s^{-1}, the fracture surfaces become rougher and local granular structures are found. The relative areas of the fracture surfaces are larger than that at low strain rates (i.e. 30.93 s^{-1} and 46.75 s^{-1}). As the strain rates further

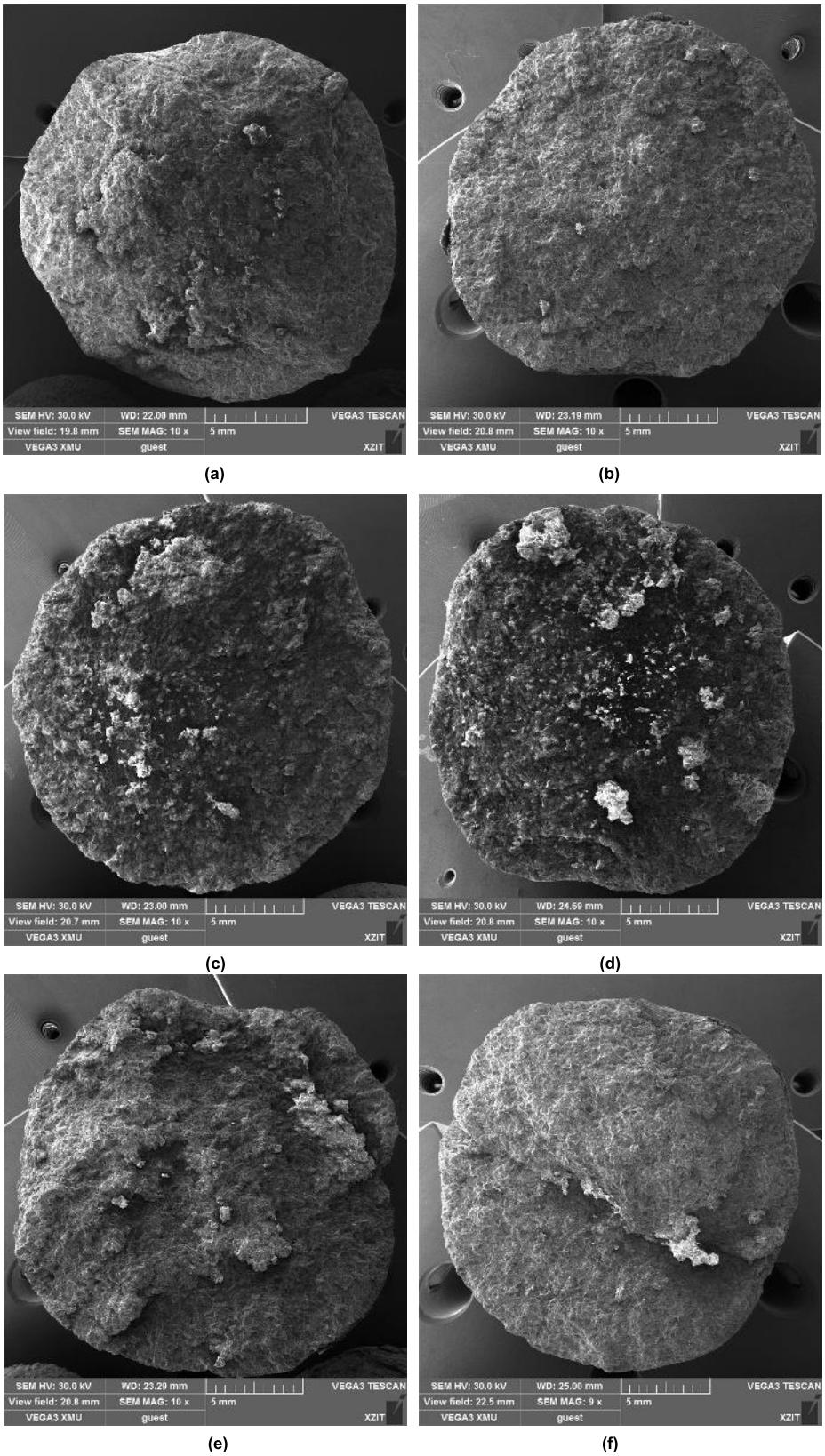

FIGURE 12. The microscopic characteristics of the fracture surfaces observed from SEM scanning (with 10-time-magnification). (a) the strain rate is 30.93s^{-1}; (b) the strain rate is 46.75s^{-1}; (c) the strain rate is 64.14s^{-1}; (d) the strain rate is 79.65s^{-1}; (e) the strain rate is 91.13s^{-1}; (f) the strain rate is 108.93 s^{-1}.

increase 91.13 s^{-1} and 108.93 s^{-1}, the fracture surfaces show typical three-dimensional structural features and uneven surfaces (that are formed by the interaction between several fractures) are found. The relative areas of the fracture surfaces also further enlarge. Therefore, according to the observation on the structural features of the fracture surfaces, the roughness of the fracture surfaces increases with the strain rates. The fracture surface changes from a relatively flat two-dimensional form to a three-dimensional form, and its relative area gradually increases.

IV. DISCUSSION

Based on the experimental results in Section 3, with the increase of the strain rate, the fracture surface of the specimen after tensile failure shows more obvious three-dimensional structural features and both the relative area and the roughness of the fracture surface gradually increase. In this section, the relation between the fracture surface roughness and the strain rate in the dynamic direct tension test is discussed through the quantitive representation of the fracture surface roughness.

A. QUANTITIVE REPRESENTATION OF FRACTURE SURFACE ROUGHNESS

The fracture surface roughness of the rock is an important parameter that describes its macroscopic fracture characteristics. The fracture surface is directly formed by the initiation and propagation of microcracks under external loading and records the damage evolution of the rock. Based on the quantitive analysis of fracture surface roughness, the energy consumption characteristics of the rock in its failure process can be understood.

1) MEASUREMENT OF THE ROUGHNESS

The high-revolution non-contact three-dimensional scanner is used to measure the roughness of the fracture surface. The JR scanner adopts the grating technology with the scan accuracy of 0.015 mm. The three-dimensional data at the fracture surface of the specimen can be obtained in a short time. The mechanism of the three-dimensional scanner is based on the unitization of the discontinuity surface. First, the heights of the 4 corner points in each tiny element are measured and the coordinates of all the tiny elements at the discontinuity surface are recorded. To eliminate the influence of the round boundary of the fracture surface on data processing, the center square area (15 mm (in length) × 15 mm (in width)) of the round fracture surface is selected for scanning. The scanning principle is illustrated in Figure 13.

The unitization results of the fracture surfaces of the specimens under dynamic direct tension at different strain rates are given in Figure 14.

2) ROUGHNESS COEFFICIENT METHOD

To represent the three-dimensional roughness of the fracture surface, the most representative method was proposed by EI-Soudani [30] who defined the roughness coefficient

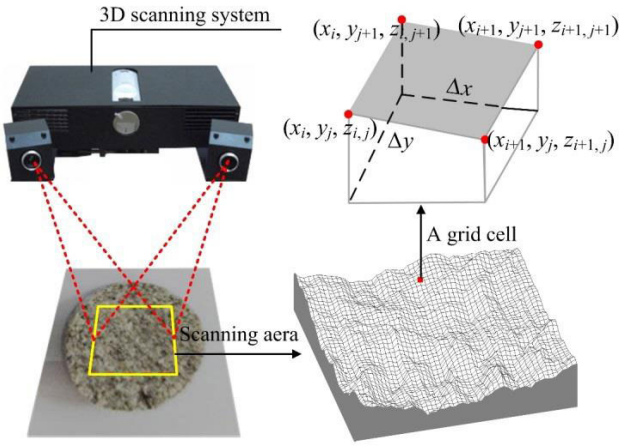

FIGURE 13. The scanning principle of the roughness of the fracture surface.

(Equation (9)) as the ratio between the actual area of the discontinuity surface and its projected area.

$$R_S = \frac{A_t}{A_n} \tag{9}$$

where R_S is the roughness coefficient, A_t is the actual area of the discontinuity surface and A_n is the projected area of the discontinuity surface.

The integration method has been proposed to calculate the actual area of the fracture surface based on the three-dimensional coordinates [43]. Its procedures are briefed below.

It is assumed that the coordinate of each point at the actual fracture surface follows a continuous differentiable function ($z = f(x, y)$). The curved surface is divided into infinite parts (n), and the unit area is defined as dS. Then the area of the fracture surface can be calculated by Equation (10).

$$S = \iint_S dS \tag{10}$$

Based on the 'replace curve by straight line' concept in calculus, a tangent plane at the fracture surface is assumed to have the same area (dA) as dS as shown in Figure 15.

Assuming the existence of the two vectors, $d\vec{u}$ and $d\vec{v}$, Equation (11) is derived and Equation (12) can be deduced to calculate the actual area of the fracture surface.

$$\begin{aligned} dA &= |d\vec{u} \times d\vec{v}| = \left\| -\frac{\partial z}{\partial x}dxdy, -\frac{\partial z}{\partial y}dxdy, dxdy \right\| \\ &= \sqrt{1 + (\frac{\partial z}{\partial x})^2 + (\frac{\partial z}{\partial y})^2}dxdy \end{aligned} \tag{11}$$

$$A_t = \int_{surface} \left\{ 1 + [\frac{\partial z}{\partial x}(x, y)]^2 + [\frac{\partial z}{\partial y}(x, y)]^2 \right\}^{1/2} dxdy \tag{12}$$

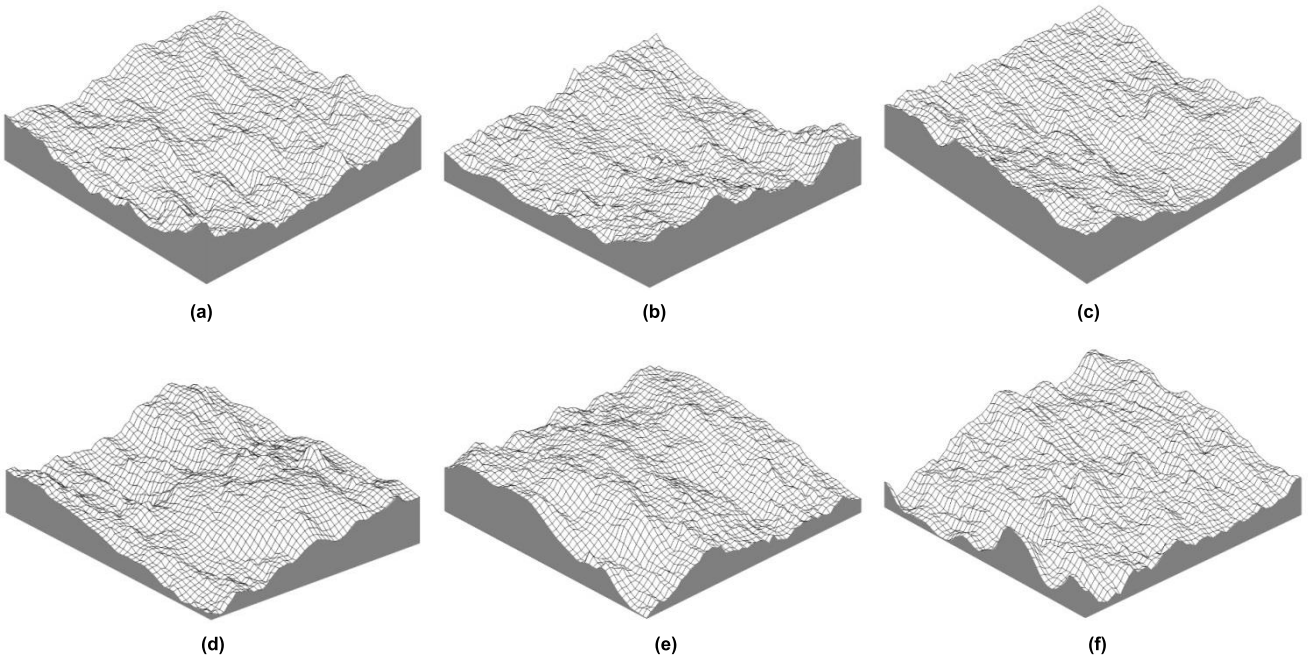

FIGURE 14. The unitization results of the fracture surfaces of the specimens under dynamic direct tension at different strain rates. (a) the strain rate is 30.93s^{-1}; (b) the strain rate is 46.75s^{-1}; (c) the strain rate is 64.14s^{-1}; (d) the strain rate is 79.65s^{-1}; (e) the strain rate is 91.13s^{-1}; (f) the strain rate is 108.93 s^{-1}.

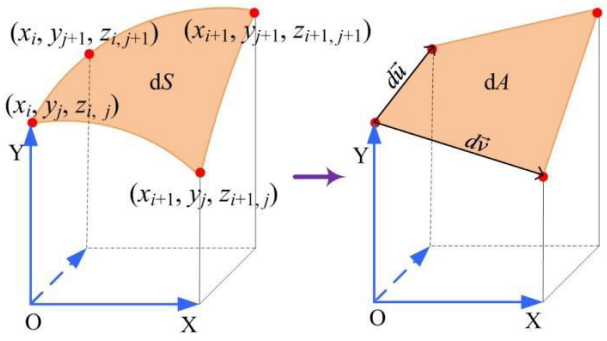

FIGURE 15. The schematic diagram of area conversion.

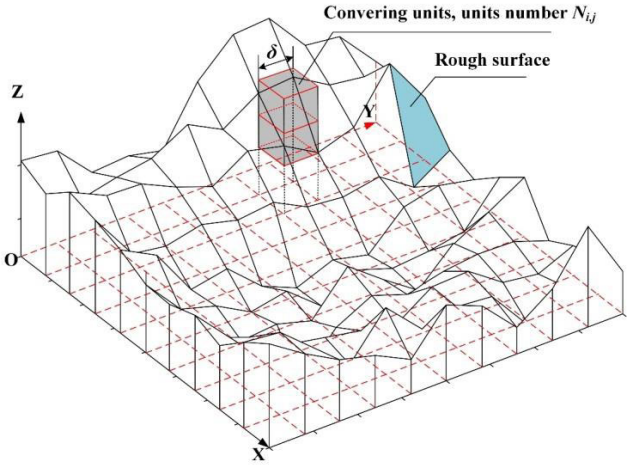

FIGURE 16. Schematic view of the cubic covering method [49].

Equation (13) is obtained if the actual area of the fracture surface is divided into elements:

$$A_t \approx (\Delta x \Delta y) \sum_{j=1}^{N_y-1} \sum_{i=1}^{N_x-1} \sqrt{1 + (\frac{z_{i+1,j} - z_{i,j}}{\Delta})^2 + (\frac{z_{i,j+1} - z_{i,j}}{\Delta})^2} \tag{13}$$

where $z_{i,j} = f\ (x_i, y_j)$, $N_x - 1$ and $N_y - 1$ is the number of intervals used for the slopes calculation.

Considering that Δx equals to Δy in the actual scanning process, a difference, Δ, is defined by Equation (14).

$$\Delta x = \Delta y = \Delta \tag{14}$$

Substituting Equation (14) into Equation (13), Equation (13) is transformed into Equation (15). Finally, the actual area of the fracture surface and the roughness coefficient can be calculated by Equations (15) and (9) respectively.

$$A_t = \Delta^2 \sum_{j=1}^{N_y-1} \sum_{i=1}^{N_x-1} \sqrt{1 + (\frac{z_{i+1,j} - z_{i,j}}{\Delta})^2 + (\frac{z_{i,j+1} - z_{i,j}}{\Delta})^2} \tag{15}$$

3) FRACTAL DIMENSION METHOD

Fractal geometry is a discipline proposed by an American mathematician named Mandelbrot in 1970s. Then it

was introduced by the Chinese Academician Heping Xie in 1990s to study the morphology of the rock fracture surface. Many previous studies revealed that the fractal dimension can be used to represent the roughness of a fracture surface [43]–[48]. The most commonly-used box-covering algorithm is used in this section to calculate the fractal dimension of the fracture surface. This algorithm utilizes three-dimensional cubes (with the size of δ) to cover the irregular element surface as shown in Figure 16. The maximum difference between the heights of the 4 corner points of each element ($(z_{i,j})$, $(z_{i+1,j})$, $(z_{i+1,j+1})$ and $(z_{i,j+1})$) determines the number of the cubes ($N_{i,j}$) used to cover this element (Equation (16)). The number of the cubes required to cover the whole fracture surface can be calculated by Equation (17).

$$N_{i,j} = \mathrm{INT} \times \left\{ \frac{1}{\delta} \begin{bmatrix} \max\left(z(i,j), z(i+1,j), z(i+1,j+1), z(i,j+1)\right) \\ -\min\left(z(i,j), z(i+1,j), z(i+1,j+1), z(i,j+1)\right) \end{bmatrix} + 1 \right\} \tag{16}$$

$$N_{(\delta)} = \sum_{i,j=1}^{n} N_{i,j} \tag{17}$$

where INT is the rounding function.

Different values of $N(\delta)$ can be derived if the size magnitude, δ, is change. Hence the relation between $N(\delta)$ and δ is given in Equation (18):

$$N_{(\delta)} \sim \delta^{-D} \tag{18}$$

where D is the fractal dimension of the fracture surface.

Based on the box-covering algorithm, Zhang *et al.* [50] proposed an improved cubic covering algorithm in which the initial position of the cube covering changes from the height of the lowest corner point to a general height. This is to avoid the complexity and miscalculation of a rough surface due to the variation of the initial position of the cube covering. Hence the roughness of the fracture surface can be more realistically reflected. The improved cubic covering algorithm is given in Equation (19), which is also the final calculation method of the fractal dimension.

$$N_{i,j} = \mathrm{INT}\left\{ \frac{1}{\delta} \left[\max\left(z(i,j), z(i+1,j), z(i+1,j+1), z(i,j+1)\right) + 1 \right] \right\} \tag{19}$$

B. ANALYSIS OF FRACTURE SURFACE ROUGHNESS

The roughness coefficients and the fractal dimensions of the fracture surfaces of the sandstone specimens under direct tension at different strain rates are provided in Table 2. The roughness coefficient and the fractal dimension of a fracture surface in Table 2 are the average results from the upper surface and the lower surface. The influence of the strain rate on the roughness coefficient and the fractal dimension

TABLE 2. Parameters reflecting the roughness of the fracture surfaces of the sandstone specimens.

Strain rate (s^{-1})	σ_T (MPa)	Average of R_S	Average of D
30.93	6.59	1.19125	2.04303
46.75	8.06	1.19243	2.04720
64.14	10.90	1.20526	2.04834
79.65	11.55	1.21098	2.04965
91.13	12.92	1.21393	2.05143
108.93	14.85	1.22416	2.05612

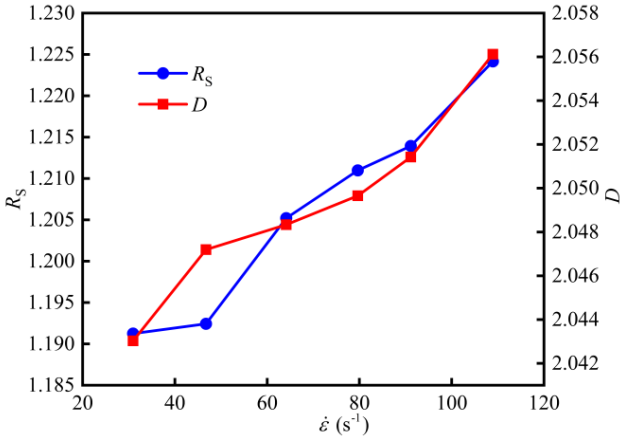

FIGURE 17. The influence of the strain rate on the roughness coefficient and the fractal dimension.

is illustrated in Figure 17. Both the roughness coefficient and the fractal dimension increase with the strain rate with a similar tendency, which shows the reliability of these two indicators on reflecting and quantifying the roughness of the fracture surface. Though the roughness coefficient and the fractal dimension of the specimen at the strain rate of 46.75 s^{-1} exhibit a quite difference, the tendency of the fracture surface roughness reflected by these two methods remains unchanged. Hence the experimental errors are deems to be within an acceptable range. The results show that the fracture surface roughness of the rock material under dynamic direct tension is notably sensitive to the strain rate. This conclusion has been rarely reported in previous studies.

Tensile strength is the maximum tensile stress the fracture surface can sustain in the fracture process, and fracture surface roughness is a direct impression of the fracture process. These two factors are closely related to each other. Therefore, the quantitive relation between tensile strength and fracture surface roughness needs to be further investigated. Figure 18 suggests that both the roughness coefficient and the fractal dimension, which reflect the roughness of the fracture surface, increase with tensile strength. The reason is that the brittle rock has a more complicated fracture propagation path in the fracture process (i.e. higher fracture surface roughness) if more energy is required for its dynamic direct tensile failure.

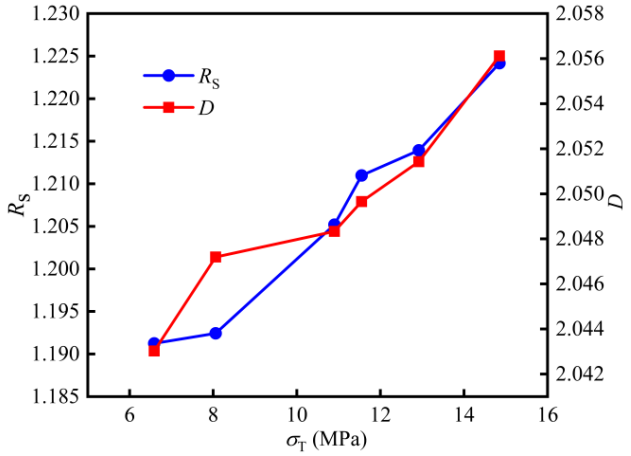

FIGURE 18. The influence of the tensile strength on the roughness coefficient and the fractal dimension.

C. RELATION BETWEEN ENERGY CONSUMPTION AND FRACTURE SURFACE ROUGHNESS OF SANDSTONE SPECIMENS IN FRACTURE PROCESSES

The energy consumption of the specimen (E) in its dynamic direct tensile failure process mainly includes two parts: the initiation energy of microcrack (E_i) and propagation energy of microcrack (E_g). Previous studies suggested that the energy consumption in the fracture process can be calculated by Equation (20) [51]–[53]:

$$E = E_i + E_g = E_i + \gamma \cdot A_t + \gamma_p \cdot v \tag{20}$$

where γ is fracture surface energy, γ_p is the average energy consumed for the plastic deformation per unit volume and v is the volume of the region sustaining plastic deformation.

The fracture energy is mainly used for the consumption of the original cracks propagation, and dynamic direct tensile failure process has few influence on the initiation energy of the cracks, so the initiation energy of microcrack can be considered as a constant [51]. During dynamic direct tensile failure process, the strain mainly occurs fracture surface of rock specimen, the plastic deformation in the rest part is tiny except fracture surface location [54]. Hence it is thought that the volume of the region sustaining plastic deformation in the direct tensile failure process is negligible. Therefore, Equation (20) can be transformed into Equation (21):

$$E = C + \gamma \cdot A_t \tag{21}$$

where C is a constant.

Substituting Equation (9) into Equation (21), Equation (22 can be derived:

$$E = C + \gamma \cdot R_S \cdot A_n \tag{22}$$

where A_n is the projected area of the fracture surface.

Therefore, Equation (22) indicates that more energy is consumed as the fracture surface roughness increases. This also suggests that the fracture surface becomes more complex with the increase of the direct tensile strength. Some assumptions are adopted in the above deduction, and the linear relation between the energy consumption and the fracture surface roughness in Equation (22) needs to be further validated by more laboratory experiments.

It should be noted that the energy consumption (E) in the above calculation is the energy consumed in the fracture process rather than the overall energy input for the tensile failure of the specimen derived from the incident signals (ε_i), the reflected signals (ε_r) and the transmission signals (ε_k) in the SHTB experiment since the latter also includes the energy released in the post-failure stage.

V. CONCLUSION

The SHTB system is used in this paper to conduct dynamic direct tensile experiments on sandstone. The roughness of the fracture surface is measured, and the mechanical characteristics and the fracture mechanism of the sandstone specimens under direct tension at different strain rates are studied. The following conclusions are made based on the experimental results.

(1) The installation of the specimen in the dynamic direct tension test is realized by adhesives and specimen reinforcement. The stress-strain curve of the specimen under dynamic direct tension is derived, which includes the elastic deformation stage, the microcrack initiation stage, the microcrack propagation stage and the unloading stage.

(2) The macroscopic mechanical properties of the specimen under direct tension are notably sensitive to the strain rate. The tensile strength, the tensile modulus and the peak strain of the specimen increase almost linearly with the strain rate. When the strain rate increases by 252 %, the tensile strength, the tensile modulus and the peak strain increase by 125 %, 37 % and 98% respectively. Based on the observation on the microscopic structural features of the fracture surfaces, it is found that the fracture surface roughness increases with the strain rate. The fracture surface of the specimen changes from a relatively flat two-dimensional state to a three-dimensional state, and its relative area gradually increases.

(3) The roughness of the fracture surfaces at different strain rates is reflected by the roughness coefficient and the fractal dimension. The reliability of these two factors on the quantitative evaluation of the fracture surface roughness is validated. It is found that the fracture surface roughness of the specimen under dynamic direct tension is significantly sensitive to the strain rate. From the aspect of energy consumption, it is manifested that both the energy consumed in the fracture process and the dynamic direct tensile strength enhance with the fracture surface roughness.

REFERENCES

[1] J. Zhang, H. Deng, J. Deng, and B. Ke, "Development of energy-based brittleness index for sandstone subjected to freeze-thaw cycles and impact loads," *IEEE Access*, vol. 6, pp. 48522–48530, 2018, doi: 10.1109/ACCESS.2018.2867349.

[2] K. Xia and W. Yao, "Dynamic rock tests using split Hopkinson (Kolsky) bar system a review," *J. Rock Mech. Geotechnical Eng.*, vol. 7, no. 1, pp. 27–59, Feb. 2015, doi: 10.1016/j.jrmge.2014.07.008.

[3] Q. He, Y. Li, J. Xu, and C. Zhang, "Prediction of mechanical properties of igneous rocks under combined compression and shear loading through statistical analysis," *Rock Mech. Rock Eng.*, vol. 53, no. 2, pp. 841–859, Feb. 2020, doi: 10.1007/s00603-019-01948-9.

[4] H. Noferesti and K. S. Rao, "Role of crystal interlocking on the strength of brittle rocks," *Rock Mech. Rock Eng.*, vol. 44, no. 2, pp. 221–230, Mar. 2011, doi: 10.1007/s00603-010-0094-5.

[5] M. Li, X. Mao, L. Cao, H. Pu, R. Mao, and A. Lu, "Effects of thermal treatment on the dynamic mechanical properties of coal measures sandstone," *Rock Mech. Rock Eng.*, vol. 49, no. 9, pp. 3525–3539, Sep. 2016, doi: 10.1007/s00603-016-0981-5.

[6] D. Li and L. N. Y. Wong, "The Brazilian disc test for rock mechanics applications: Review and new insights," *Rock Mech. Rock Eng.*, vol. 46, no. 2, pp. 269–287, Mar. 2013, doi: 10.1007/s00603-012-0257-7.

[7] N. Huang, R. Liu, Y. Jiang, B. Li, and L. Yu, "Effects of fracture surface roughness and shear displacement on geometrical and hydraulic properties of three-dimensional crossed rock fracture models," *Adv. Water Resour.*, vol. 113, pp. 30–41, Mar. 2018, doi: 10.1016/j.advwatres.2018.01.005.

[8] M. Mousavi Nezhad, Q. J. Fisher, E. Gironacci, and M. Rezania, "Experimental study and numerical modeling of fracture propagation in shale rocks during Brazilian disk test," *Rock Mech. Rock Eng.*, vol. 51, no. 6, pp. 1755–1775, Jun. 2018, doi: 10.1007/s00603-018-1429-x.

[9] F. Dai, S. Huang, K. Xia, and Z. Tan, "Some fundamental issues in dynamic compression and tension tests of rocks using split Hopkinson pressure bar," *Rock Mech. Rock Eng.*, vol. 43, no. 6, pp. 657–666, Nov. 2010, doi: 10.1007/s00603-010-0091-8.

[10] M. Li, X. B. Mao, H. Pu, Y. L. Chen, Y. Wu, and L. Y. Zhang, "Effects of heating rate on the dynamic tensile mechanical properties of coal sandstone during thermal treatment," *Shock Vib.*, vol. 2017, Oct. 2017, Art. no. 4137805, doi: 10.1155/2017/4137805.

[11] T. Yin, X. Li, W. Cao, and K. Xia, "Effects of thermal treatment on tensile strength of Laurentian granite using Brazilian test," *Rock Mech. Rock Eng.*, vol. 48, no. 6, pp. 2213–2223, Nov. 2015, doi: 10.1007/s00603-015-0712-3.

[12] H. B. Li, J. W. Zhang, W. Shao, and J. R. Li, "Mechanical properties of Bukit Timah granite under dynamic tension," *Rock Soil Mech.*, vol. 23, no. S1, pp. 1–4, Oct. 2002, doi: 10.16285/j.rsm.2002.s1.034.

[13] Y. Xu, F. Dai, N.-W. Xu, T. Zhao, and C. Zhou, "Discrete element simulation of dynamic semi-circular bend flexure tests of rocks using split hopkinson pressure bar," *Arabian J. Geosci.*, vol. 9, no. 9, pp. 1–13, Jul. 2016, doi: 10.1007/s12517-016-2574-8.

[14] F. Dai, K. Xia, and L. Tang, "Rate dependence of the flexural tensile strength of Laurentian granite," *Int. J. Rock Mech. Mining Sci.*, vol. 47, no. 3, pp. 469–475, Apr. 2010, doi: 10.1016/j.ijrmms.2009.05.001.

[15] X. Yu, C. Da Gama, Y. Na, Q. Wang, and Q. Xie, "Deformation behaviour of rocks under compression and direct tension," *J. Southern Afr. Inst. Mining Metall.*, vol. 105, no. 1, pp. 55–62, Jan. 2005.

[16] K. Zhang, R. G. Chen, W. Zhang, and X. Q. Jiang, "Study of experimental technique for concrete dynamic direct tension," *J. Exp. Mech.*, vol. 29, no. 1, pp. 89–96, Feb. 2014, doi: 10.7520/1001-4888-13-064.

[17] H. Lan, J. Chen, and R. Macciotta, "Universal confined tensile strength of intact rock," *Sci. Rep.*, vol. 9, no. 1, pp. 6170–6179, Apr. 2019, doi: 10.1038/s41598-019-42698-6.

[18] H. Li, J. Li, B. Liu, J. Li, S. Li, and X. Xia, "Direct tension test for rock material under different strain rates at quasi-static loads," *Rock Mech. Rock Eng.*, vol. 46, no. 5, pp. 1247–1254, Sep. 2013, doi: 10.1007/s00603-013-0406-7.

[19] D. Saiang, L. Malmgren, and E. Nordlund, "Laboratory tests on shotcrete-rock joints in direct shear, tension and compression," *Rock Mech. Rock Eng.*, vol. 38, no. 4, pp. 275–297, Sep. 2005, doi: 10.1007/s00603-005-0055-6.

[20] Q. Zhang, K. Duan, W. Xiang, S. Yuan, and Y.-Y. Jiao, "Direct tensile test on brittle rocks with the newly developed centering apparatus," *Geotechnical Test. J.*, vol. 41, no. 1, Jan. 2018, Art. no. 20160301, doi: 10.1520/GTJ20160301.

[21] T. Unlu and O. Yilmaz, "Development of a new push–pull direct tensile strength testing apparatus (PPTA)," *Geotechnical Test. J.*, vol. 37, no. 1, Jan. 2014, Art. no. 20130040, doi: 10.1520/GTJ20130040.

[22] J. Liu, C. Wang, Z. Wu, L. Wang, H. Xu, J. Pei, and C. Deng, "A new approach of rock tension-compression cyclic measurement," *Géotechnique Lett.*, vol. 9, no. 2, pp. 89–93, Jun. 2019, doi: 10.1680/jgele.18.00202.

[23] K. Hashiba, T. Okada, K. Tani, S. Shirasagi, K. Hayano, T. Nakamura, hboxY. Oikawa, M. Ono, K. Shimamoto, and S. Yamada, "Literature survey and experimental study on the direct tension test on rocks," *Geotech. Test. J.*, vol. 40, no. 2, pp. 806–815, May 2017, doi: 10.1520/GTJ20160201.

[24] P. Yin, H. C. Ma, X. W. Liu, J. Bi, X. P. Zhou, and F. Berto, "Numerical study on the dynamic fracture behavior of 3D heterogeneous rocks using general particle dynamics," *Theor. Appl. Fract. Mech.*, vol. 96, pp. 90–104, Aug. 2018, doi: 10.1016/j.tafmec.2018.04.005.

[25] Z. Y. Liao, J. B. Zhu, K. W. Xia, and C. A. Tang, "Determination of dynamic compressive and tensile behavior of rocks from numerical tests of split hopkinson pressure and tension bars," *Rock Mech. Rock Eng.*, vol. 49, no. 10, pp. 3917–3934, Oct. 2016, doi: 10.1007/s00603-016-0954-8.

[26] E. Cadoni, "Dynamic characterization of orthogneiss rock subjected to intermediate and high strain rates in tension," *Rock Mech. Rock Eng.*, vol. 43, no. 6, pp. 667–676, May 2010, doi: 10.1007/s00603-010-0101-x.

[27] X. Z. Kong, Q. Fang, and J. Hong, "A new damage-based nonlocal model for dynamic tensile failure of concrete material," *Int. J. Impact Eng.*, vol. 132, no. 10, Oct. 2019, Art. no. 103336, doi: 10.1016/j.ijimpeng.2019.103336.

[28] K. Takahashi, M. Kido, and K. Arakawa, "Fracture roughness evolution during mode I dynamic crack propagation in brittle materials," *Int. J. Fract.*, vol. 90, nos. 1–2, pp. 119–131, Jan. 1998, doi: 10.1023/a:1007443419107.

[29] N. Barton, "Review of a new shear-strength criterion for rock joints," *Eng. Geol.*, vol. 7, no. 4, pp. 287–332, Nov. 1973, doi: 10.1016/0013-7952(73)90013-6.

[30] S. M. El-Soudani, "Profilometric analysis of fractures," *Metallography*, vol. 11, no. 3, pp. 247–336, Jul. 1978, doi: 10.1016/0026-0800(78)90045-9.

[31] N. H. Maerz, J. A. Franklin, and C. P. Bennett, "Joint roughness measurement using shadow profilometry," *Int. J. Rock Mech. Mining Sci. Geomech. Abstr.*, vol. 27, no. 5, pp. 329–343, Oct. 1990, doi: 10.1016/0148-9062(90)92708-M.

[32] J. Zhao, "Joint surface matching and shear strength part B: JRC-JMC shear strength criterion," *Int. J. Rock Mech. Min.*, vol. 34, no. 2, pp. 179–185, Feb. 1997, doi: 10.1016/S0148-9062(96)00063-0.

[33] G. Rong, J. Yang, L. Cheng, J. Tan, J. Peng, and C. Zhou, "A Forchheimer equation-based flow model for fluid flow through rock fracture during shear," *Rock Mech. Rock Eng.*, vol. 51, no. 9, pp. 2777–2790, Sep. 2018, doi: 10.1007/s00603-018-1497-y.

[34] R. Tse and D. M. Cruden, "Estimating joint roughness coefficients," *Int. J. Rock Mech. Mining Sci. Geomech. Abstr.*, vol. 16, no. 5, pp. 303–307, Oct. 1979, doi: 10.1016/0148-9062(79)90241-9.

[35] E. T. Brown, Ed., *Rock Characterization, Testing and Monitoring: ISRM Suggested Methods* (Suggested Methods for the Quantitative Description of Discontinuities in Rock Masses). Oxford, U.K.: Pergamon, 1981, pp. 3–52.

[36] G. Rong, J. Yang, L. Cheng, and C. Zhou, "Laboratory investigation of nonlinear flow characteristics in rough fractures during shear process," *J. Hydrol.*, vol. 541, pp. 1385–1394, Oct. 2016, doi: 10.1016/j.jhydrol.2016.08.043.

[37] Y. Xu and F. Dai, "Dynamic response and failure mechanism of brittle rocks under combined compression-shear loading experiments," *Rock Mech. Rock Eng.*, vol. 51, no. 3, pp. 747–764, Mar. 2018, doi: 10.1007/s00603-017-1364-2.

[38] H. B. Du, F. Dai, Y. Xu, Z. L. Yan, and M. D. Wei, "Mechanical responses and failure mechanism of hydrostatically pressurized rocks under combined compression-shear impacting," *Int. J. Mech. Sci.*, vol. 165, no. 1, Jan. 2020, Art. no. 105219, doi: 10.1016/j.ijmecsci.2019.105219.

[39] H.-B. Du, F. Dai, Y. Xu, Y. Liu, and H.-N. Xu, "Numerical investigation on the dynamic strength and failure behavior of rocks under hydrostatic confinement in SHPB testing," *Int. J. Rock Mech. Mining Sci.*, vol. 108, pp. 43–57, Aug. 2018, doi: 10.1016/j.ijrmms.2018.05.008.

[40] P. Pei, F. Dai, Y. Liu, and M. Wei, "Dynamic tensile behavior of rocks under static pre-tension using the flattened Brazilian disc method," *Int. J. Rock Mech. Mining Sci.*, vol. 126, Feb. 2020, Art. no. 104208, doi: 10.1016/j.ijrmms.2019.104208.

[41] J. Liu, S. Song, X. Cao, Q. Meng, H. Pu, Y. Wang, and J. Liu, "Determination of full-scale pore size distribution of gaomiaozi bentonite and its permeability prediction," *J. Rock Mech. Geotech. Eng.*, vol. 12, no. 2, pp. 403–413, Apr. 2020, doi: 10.1016/j.jrmge.2019.12.005.

[42] S. B. Song, J. F. Liu, H. Y. Ni, X. L. Cao, H. Pu, and B. X. Huang, "A new automatic thresholding algorithm for unimodal gray-level distribution images by using the gray gradient information," *J. Petroleum Sci. Eng.*, vol. 190, no. 7, Jul. 2020, Art. no. 107074, doi: 10.1016/j.petrol.2020.107074.
[43] T. Belem, F. Homand-Etienne, and M. Souley, "Quantitative parameters for rock joint surface roughness," *Rock Mech. Rock Eng.*, vol. 33, no. 4, pp. 217–242, Oct. 2000, doi: 10.1007/s006030070001.
[44] T. Ai, R. Zhang, H. W. Zhou, and J. L. Pei, "Box-counting methods to directly estimate the fractal dimension of a rock surface," *Appl. Surf. Sci.*, vol. 314, pp. 610–621, Sep. 2014, doi: 10.1016/j.apsusc.2014.06.152.
[45] T. Babadagli, X. Ren, and K. Develi, "Effects of fractal surface roughness and lithology on single and multiphase flow in a single fracture: An experimental investigation," *Int. J. Multiphase Flow*, vol. 68, pp. 40–58, Jan. 2015, doi: 10.1016/j.ijmultiphaseflow.2014.10.004.
[46] Y. Ge, P. H. S. W. Kulatilake, H. Tang, and C. Xiong, "Investigation of natural rock joint roughness," *Comput. Geotechnics*, vol. 55, pp. 290–305, Jan. 2014, doi: 10.1016/j.compgeo.2013.09.015.
[47] G. Grasselli and P. Egger, "Constitutive law for the shear strength of rock joints based on three-dimensional surface parameters," *Int. J. Rock Mech. Mining Sci.*, vol. 40, no. 1, pp. 25–40, Jan. 2003, doi: 10.1016/S1365-1609(02)00101-6.
[48] Y. Li and R. Huang, "Relationship between joint roughness coefficient and fractal dimension of rock fracture surfaces," *Int. J. Rock Mech. Mining Sci.*, vol. 75, pp. 15–22, Apr. 2015, doi: 10.1016/j.ijrmms.2015.01.007.
[49] H. W. Zhou and H. Xie, "Direct estimation of the fractal dimensions of a fracture surface of rock," *Surf. Rev. Lett.*, vol. 10, no. 5, pp. 751–762, Oct. 2003, doi: 10.1142/s0218625x03005591.
[50] Y. H. Zhang, H. W. Zhou, and H. P. Xie, "Improved cubic covering method for fractal dimensions of a fracture surface of rock," *Chin. J. Rock Mech. Eng.*, vol. 24, no. 17, pp. 3192–3196, Sep. 2005, doi: 10.3321/j.issn:1000-6915.2005.17.030.
[51] P. Du, B. Xue, Y. Song, S. Lu, J. Yu, and Q. Zheng, "Fracture surface characteristics and impact properties of poly(butylene terephthalate)," *Polym. Bull.*, vol. 64, no. 2, pp. 185–196, Jan. 2010, doi: 10.1007/s00289-009-0199-8.
[52] Z. Luo, T. Xu, J. Yu, and Y. C. Liu, "The relationship between fracture energy and characteristic area and roughness of PVC section," *Acta Polym. Sinica*, no. 4, pp. 494–497, Aug. 1999, doi: 10.3321/j.issn:1000-3304.1999.04.020.
[53] J. Yu, Z. H. Jin, H. Lei, Y. C. Liu, and Z. Luo, "The quantitative relation between notched impact strength and fracture surface roughness of polymer materials," *Acta Polym. Sinica*, vol. 43, no. 5, pp. 612–615, Oct. 1999, doi: 10.3321/j.issn:1000-3304.1999.04.020.
[54] Z. Y. Liao, J. B. Zhu, and C. A. Tang, "Numerical investigation of rock tensile strength determined by direct tension, Brazilian and three-point bending tests," *Int. J. Rock Mech. Mining Sci.*, vol. 115, no. 3, pp. 21–32, Mar. 2019, doi: 10.1016/j.ijrmms.2019.01.007.

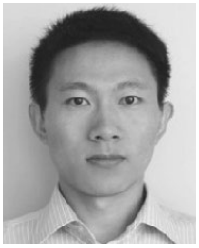

YANLONG CHEN was born in Chengde, Hebei, China, in 1982. He received the B.S. and M.S. degrees in mining engineering from the China University of Mining and Technology, Xuzhou, Jiangsu, China, in 2007 and 2010, respectively, and the Ph.D. degree in earth resources from the School of Engineering, Kyushu University, Fukuoka, Japan, in 2013.

From 2014 to 2017, he was a Lecturer, and since 2018, he has been an Associate Professor with the State Key Laboratory for Geomechanics and Deep Underground Engineering, China University of Mining and Technology. His main research interests include rock mechanics and mining engineering.

GANG LIN was born in Lu'an, Anhui, China, in 1996. He received the B.S. degree in mining engineering from the Anhui University of Science and Technology, Huainan, Anhui, in 2018. He is currently pursuing the M.S. degree in engineering mechanics with the China University of Mining and Technology, Xuzhou, Jiangsu, China.

His main research interests include rock dynamics and the damage characteristics of rock material.

RONGRONG MAO was born in Qidong, Jiangsu, China, in 1980. She received the Ph.D. degree in engineering mechanics from the China University of Mining and Technology, Xuzhou, Jiangsu, in 2019.

She is currently a Lecturer with the Department of Ship and Marine Engineering, Nantong Shipping College, Nantong, Jiangsu. Her main research interest includes rock dynamics.

MING LI was born in Yishui, Shandong, China, in 1986. He received the B.S. and Ph.D. degrees from the China University of Mining and Technology, Xuzhou, Jiangsu, China.

He is currently an Associate Professor with the State Key Laboratory for Geomechanics and Deep Underground Engineering, China University of Mining and Technology. His main research interests include rock mechanics and rock dynamics.

XIANBIAO MAO was born in Qidong, Jiangsu, China, in 1959. He received the B.S., M.S., and Ph.D. degrees from the China University of Mining and Technology, Xuzhou, Jiangsu.

He is currently a Professor and a Doctoral Supervisor with the China University of Mining and Technology. His main research interest includes rock mechanics.

KAI ZHANG was born in Zhoukou, Henan, China, in 1984. He received the B.S. degree in engineering mechanics from the China University of Mining and Technology, in 2005, and the Ph.D. degree in rock mechanics from the Institute of Rock and Soil Mechanics, Chinese Academy of Sciences, in 2010.

He is currently a Professor and a Doctoral Supervisor with the China University of Mining and Technology. His main research interests include geomechanics and underground engineering.